LETTERS
PUBLISHED ONLINE: 20 NOVEMBER 2011 | DOI: 10.1038/NMAT3169
nature materials

Synthesis of monolithic graphene–graphite integrated electronics

Jang-Ung Park[1]*†, SungWoo Nam[2,3]*†, Mi-Sun Lee[1] and Charles M. Lieber[2,3]

Encoding electronic functionality into nanoscale elements during chemical synthesis has been extensively explored over the past decade as the key to developing integrated nanosystems[1] with functions defined by synthesis[2–6]. Graphene[7–12] has been recently explored as a two-dimensional nanoscale material, and has demonstrated simple device functions based on conventional top-down fabrication[13–20]. However, the synthetic approach to encoding electronic functionality and thus enabling an entire integrated graphene electronics in a chemical synthesis had not previously been demonstrated. Here we report an unconventional approach for the synthesis of monolithically integrated electronic devices based on graphene and graphite. Spatial patterning of heterogeneous metal catalysts permits the selective growth of graphene and graphite, with a controlled number of graphene layers. Graphene transistor arrays with graphitic electrodes and interconnects were formed from the synthesis. These functional, all-carbon structures were transferable onto a variety of substrates. The integrated transistor arrays were used to demonstrate real-time, multiplexed chemical sensing and more significantly, multiple carbon layers of the graphene–graphite device components were vertically assembled to form a three-dimensional flexible structure which served as a top-gate transistor array. These results represent substantial progress towards encoding electronic functionality through chemical synthesis and suggest the future promise of one-step integration of graphene–graphite based electronics.

We demonstrate that differences in the carbon solubility of metal catalyst films can be used to synthesize different thicknesses of graphene and graphite, and such catalyst films can be patterned, thus enabling graphene and graphite patterns to be produced in localized and selected areas. For example, a Ni or Co film has relatively high solubility of carbon ($\gtrsim$1.3 at.% at 1,000 °C) and can produce graphite by segregation and precipitation of the carbon on the metal surface[18,19]. In comparison, Cu film has almost negligible carbon solubility (<0.0001 at.% at 1,000 °C) and can generate ~1–3 graphene layers by carbon adsorption on a Cu surface[17,21].

Figure 1a illustrates the patterned catalyst films before the chemical vapour deposition (CVD) synthesis. Co and Ni were deposited as consonant and vowel alphabet structures, respectively, on a Cu film that was coated with a thin Ni protection top layer against Cu oxidation. As the temperature increased up to 1,000 °C during CVD synthesis, the deposited Co and Ni diffused locally into the Cu layer to form alloys (Supplementary Fig. S1). After the synthesis and catalyst metal layer removal, the monolithic graphene–graphite structure was transferred to 285 nm-thick SiO_2 on a Si substrate (Fig. 1b) (see Methods and Supplementary Information). The different colours and contrasts shown by the three areas in Fig. 1b (consonant, vowel and background) are due to the fact that the reflectance at the air/graphene multilayers and graphene multilayers/SiO_2 interfaces varies with the number of graphene layers[22].

Raman spectra from these three different graphene–graphite regions (Fig. 1c) exhibited three characteristic bands (D: centred at ~1,350 cm^{-1}, G: centred at ~1,590 cm^{-1}, 2D: centred at ~2,680 cm^{-1}) of graphene and graphite. The background region (synthesized from Cu) predominantly showed a G band intensity comparable to the 2D band intensity, indicating two graphene layers[17,23]. We also observed layer variations[24,25], and atomic force microscopy (AFM) measurements of step heights that further confirmed the thickness of 2–4 layers (<1.7 nm). Raman spectra obtained from the consonant area (Fig. 1c) showed that the G band intensity was enhanced significantly and the 2D band became non-symmetric and dispersive (broader), with a slight blueshift due to interlayer binding, when compared with the vowel region. This observation indicates that the thickness of the consonant area is thicker than the thickness of the vowel area[17,23], which was further confirmed by AFM measurements showing granular graphite grains with a thickness of ~40–190 nm in the consonant areas and relatively thinner graphite with a thickness of ~2 ± 0.94 nm (~6–8 layers) in the vowel areas. Phase separation of the Co–Cu alloy system occurs in the synthesis, and the consonant patterns contained both small graphite grains and few-layer graphene areas synthesized together from Co-rich and Cu-rich phases, respectively. We also observed that the size of the graphite grains increased with the thickness of the Co catalyst (Supplementary Fig. S2) and that film-like graphitic structures (thickness: ~300 ± 63 nm), with negligible areas of few-layer graphene, were synthesized when the Co catalyst was thick enough (thickness: $\gtrsim$400 nm).

Figure 1d shows two-dimensional maps of the G and 2D bands scanned on the synthesized area indicated by the red-dashed square in Fig. 1a. Both G and 2D band mapping of the thick graphite region of the letter 'r' showed a distinctive intensity contrast following the original catalyst pattern (Fig. 1d). Furthermore, the mapping results showed that the graphite pattern was continuous and connected to the background 2–4-layer graphene, which clearly demonstrated monolithic synthesis of differing thicknesses. The cross-sectional transmission electron microscope (TEM) images (Supplementary Fig. S3a) further verified that the number of layers changes gradually at the interface between graphene and graphite with a uniform

[1]School of Nano-Biotechnology and Chemical Engineering, School of Mechanical and Advanced Materials Engineering, Graphene Research Center, Ulsan National Institute of Science and Technology (UNIST), Ulsan Metropolitan City, 689-798, Republic of Korea, [2]Department of Chemistry and Chemical Biology, Harvard University, Cambridge, Massachusetts 02138, USA, [3]School of Engineering and Applied Sciences, Harvard University, Cambridge, Massachusetts 02138, USA. †These authors contributed equally to this work. *e-mail: jangung@unist.ac.kr; nam@cmliris.harvard.edu.

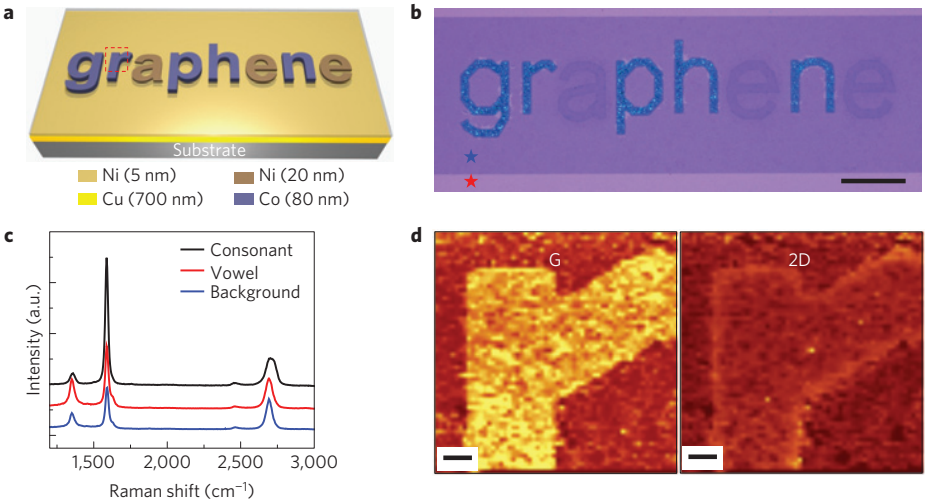

Figure 1 | Synthesis of monolithic graphene–graphite structures using heterogeneously patterned metal catalyst films. a, Schematic illustration of alphabetic catalyst patterns. **b**, Optical micrograph of the graphene–graphite structures synthesized from the catalysts shown in **a**. The areas marked with red and blue stars represent SiO_2 and 2–4-layer graphene, respectively. Scale bar, 200 μm. **c**, Raman spectra from different regions (consonant, vowel, and background). **d**, Raman intensity maps of G (1,537–1,624 cm^{-1}) and 2D (2,632–2,778 cm^{-1}) bands in the region of alphabet pattern 'r'. Scale bars, 10 μm.

interlayer spacing. TEM characterization indicated that the graphite and graphene had formed a continuous interface. Supplementary Fig. S3b and S3c represents hexagonal, electron diffraction patterns of the graphene and graphite from selected areas, respectively. Supplementary Fig. S4 shows energy dispersive X-ray analysis (EDAX) and X-ray photoelectron spectroscopy (XPS) analysis of the monolithic graphene–graphite transferred onto a Si wafer with a 285 nm-thick SiO_2 layer after the removal of metal catalysts (Cu, Ni, and Co). No characteristic peaks from the metals were detected, which indicated that metal catalysts were completely removed by the etching process.

The electrical properties of graphene and graphite can be modulated by controlling the number of graphene layers (n). First, we show that conductivity or sheet resistance can be controlled by more than an order of magnitude, dependent on n. Films of graphene and graphite with different values of n were synthesized using different metal catalyst films, as previously described (also see Methods and Supplementary Information). Figure 2a shows the sheet resistance values of graphene and graphite measured using a four-point probe as a function of n. The sheet resistance was reduced by a factor of about 25 (from $2{,}463 \pm 1{,}037\ \Omega$/sq down to $98 \pm 46\ \Omega$/sq) as n increased from ~2–4 to ~850 layers. Local variations of n influence the deviation of the sheet resistance. We also characterized the field-effect response of both 2–4-layer graphene and ~850 layer graphite (Supplementary Fig. S5). The current versus back-gate characteristics showed much stronger modulation in 2–4-layer graphene, compared with a negligible change in the thick graphite (~850 layers) owing to the stronger screening effect as the number of layers increases[26]. The low sheet resistance and field-effect response of graphite are advantageous for applications in conductive films or electrodes. In contrast, the superior transconductance level of the 2–4-layer graphene is appropriate for the active channels of field-effect transistors (FETs).

The capability to modulate electronic properties through the synthetic control of the graphite thickness provides a route towards the rational design and synthesis of large-scale electronics based entirely on carbon. The metal catalyst, Cu/Ni (700 nm/5 nm), was used to synthesize 2–4-layer graphene channels and the same combination with an additional Co (400 nm) was used to produce graphite electrodes which serve as the source (S) and drain (D) (Fig. 2b). This method enabled the fabrication of all-carbon-based transistor arrays which were then transferred onto 285 nm-thick SiO_2 on a Si wafer for measurement of the back-gate response. A Raman map (G band) of the monolithic graphene–graphite FET and an AFM scan of the interface between the graphene channel and the graphite electrode are demonstrated in Fig. 2c and Supplementary Fig. S6, respectively. S/D current (I_D) versus back-gate bias (V_G) characterization of these FETs was performed at room temperature (Fig. 2d, black curve), which showed ambipolar behaviour consistent with the expected semimetallic characteristics of graphene[7,8,17,18], with a positive charge neutrality point of ~11 V. After a thermal annealing step to remove the resist residues, our monolithic graphene–graphite FET showed an improved hole (electron) mobility of ~1,800 (1,400) $cm^2\ V^{-1}\ s^{-1}$ (Fig. 2d, red curve), calculated using a standard metal-oxide-semiconductor FET model. The evaporated Cu layer can cause dewetting of Cu on SiO_2/Si at the synthesis temperature, which can induce locally empty areas of the catalyst and defects in graphene, leading to reduced mobility values[16]. The reduction of the defects in graphene[17,27], the optimization of the growth and transfer conditions[24,25], and the choice of substrates[28] with reduced roughness and chemical reactivity can further enhance the performance of our monolithic graphene–graphite FETs. The electrical properties of the interface between the graphene channel and the graphite electrodes were compared against those of the interface between the graphene and Cr/Au metals (Cr: 2 nm and Au 100 nm), as presented in Fig. 2e. The I–V characteristics for both cases showed similar linear characteristics at room temperature, presenting no Schottky contact behaviour. The contact resistances of the graphene–metal (Cr/Au) junctions and the monolithic graphene–graphite were estimated at 300 K using the transfer length method (Supplementary Fig. S7). Covalent graphite contacts to the graphene channels exhibit similar or slightly lower contact resistances (~700–900 Ω μm) compared with those of Cr/Au (~1,100 Ω μm). Furthermore, our investigation showed that the graphite contacts with ~100 and ~300 nm thickness do not exhibit a significant difference in contact resistance. As well as the properties of the contact between the graphite electrode and the graphene channel, an advantage of graphite over metals lies in its superb mechanical flexibility. We observed that even when graphite electrodes were distorted up to a strain of ~2%, the I–V characteristics remained the same (Fig. 2f).

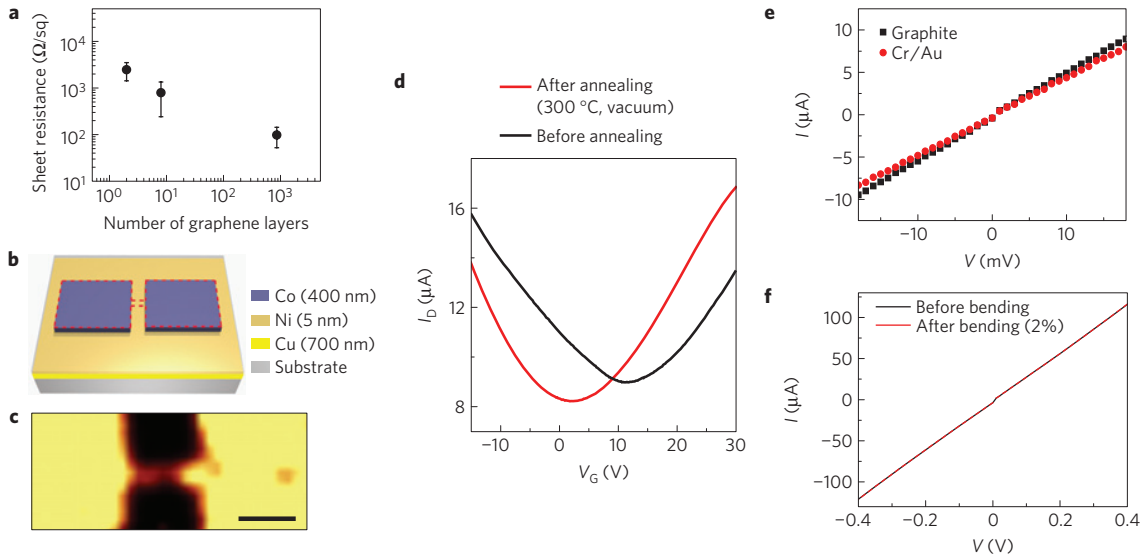

Figure 2 | Synthesis and electrical characteristics of monolithic graphene–graphite back-gate FETs. a, Sheet resistance as a function of the number of graphene layers (n). The error bars represent one standard deviation. **b**, Schematic illustration of the catalyst pattern used to synthesize the monolithic FET. Red-dashed lines indicate the masked area against O_2 plasma etching for device isolation after the CVD synthesis. **c**, Raman map (G band) of the graphene channel area with the graphitic source/drain after the isolation step (channel width: 1 μm, length: 4 μm). Scale bar, 5 μm. **d**, I_D–V_G characteristics of a monolithic graphene–graphite back-gate FET (V_D: 0.1 V). **e**, Comparison of contact properties (1) between the monolithic graphene channel and the graphite electrodes (black square) and (2) between graphene and the Cr (2 nm) / Au (100 nm) electrodes evaporated on graphene (red), with identical dimensions of the electrode pads and the channel. **f**, Electrical characterization (I–V) of the graphite electrodes before and after elastic bending/distortion (strain of ~2%). The thickness of the graphite electrodes in **c**–**f** is ~300 ± 63 nm.

The synthetic method facilitated the creation of large-scale field-effect sensor arrays composed of monolithic graphene–graphite, which were transferred onto 285 nm SiO_2 on Si wafers. Each block of the array contained nine of the 2–4-layer graphene field-effect sensors with a graphite single common source and independent drains. The sensor chip had four of these blocks composed of 36 sensor devices in total, as illustrated in Fig. 3a. The graphite electrode areas were covered with a 2 μm-thick SU8 passivation layer with openings around the 2–4-layer graphene channels. The current change measured while sweeping the Ag/AgCl water-gate voltage for different solution pH is presented in Fig. 3b. The charge neutrality point shifted positively with increasing pH; the pH sensitivity was ~17 mV/pH. These monolithic devices with synthesized graphite electrodes showed similar sensitivity levels to graphene sensors fabricated by standard lithography using evaporated metal electrodes[29,30]. However, compared with the previous reports using mechanically exfoliated graphene[29,30], our regular sensor arrays, with an integrated geometry including interconnects, obtained by synthesis demonstrated an advantage in creating multiplexed sensor arrays. The water-gate response (Fig. 3b) exhibited ambipolar characteristics, showing the possibility of complementary sensing in both the p-type and n-type regimes. Statistical distributions of the normalized transconductance and charge neutrality point at pH 7 for the device array are shown in Fig. 3c,d. Gaussian fits of the two device parameters indicated centre values of the normalized transconductance and charge neutrality point as $540 \pm 199\,\mu S\,V^{-1}$ and -0.03 ± 0.038 V, respectively. Real-time multiplexed pH sensing using the nine field-effect sensor array is demonstrated in Fig. 3e. The conductance increased (decreased) on switching solutions to higher (lower) pH in the p-type regime (water-gate potential: −0.1 V), with inverted responses observed in the n-type regime (0.3 V) as complementary sensing. The complementary sensing capability of graphene field-effect sensors has advantages over other unipolar field-effect sensors[30] as it enables the discrimination of possible electrical cross-talk and/or false-positive signals. Furthermore, the hydrophobic nature and high elastic modulus of the graphene/graphite enable entire, monolithic arrays in a free-standing form to float sustainably on water (Fig. 3f). By transferring the floating arrays, integrated device structures of monolithic graphene–graphite can be formed on various non-planar substrates. As examples, Fig. 3g demonstrates monolithic devices wrapped on the outside surfaces of a thin cylindrical glass tube (outer diameter: ~1.5 mm), an eye contact lens (soft galyfilcon A polymer), a glove finger (latex), a coin, and three different body areas of an insect (*Odontolabis sarasinorum* specimen).

Flexible electronics represents an important application area that can take advantage of monolithically integrated graphene–graphite devices. We demonstrate the capabilities of assembling multiple layers of the synthesized graphene–graphite device components vertically as 3D integration on plastic films (Fig. 4 and Supplementary Fig. S8). To realize this fabrication, monolithically integrated graphene–graphite structures (2–4-layer graphene FET channel with ~850 layer graphite S/D and interconnects using a pattern shape similar to Fig. 3f) were transferred onto a polyether ether ketone (PEEK) film, followed by deposition of a SiO_2 dielectric layer. By assembling a graphitic (~6–8 graphene layers) top-gate layer on the SiO_2, flexible monolithic FET arrays were completed (see Methods and Supplementary Information). Figure 4a,b shows schematic illustrations of the device layouts and an optical micrograph of the devices wrapped on a cylindrical glass support (radius of curvature: 1.2 cm). As well as mechanical flexibility, optical transparency is another important characteristic of our monolithically integrated graphene–graphite circuits. As shown in the left inset of Fig. 4b, the underlying paper printed with a logo was clearly visible through the semitransparent top-gated devices that were positioned on top of the paper. The transmittance of single-layer graphene is ~97% at 550 nm wavelength and decreases for higher n (ref. 24). Therefore the overall transparency of the monolithic devices can be adjusted by the value of n for each device com-

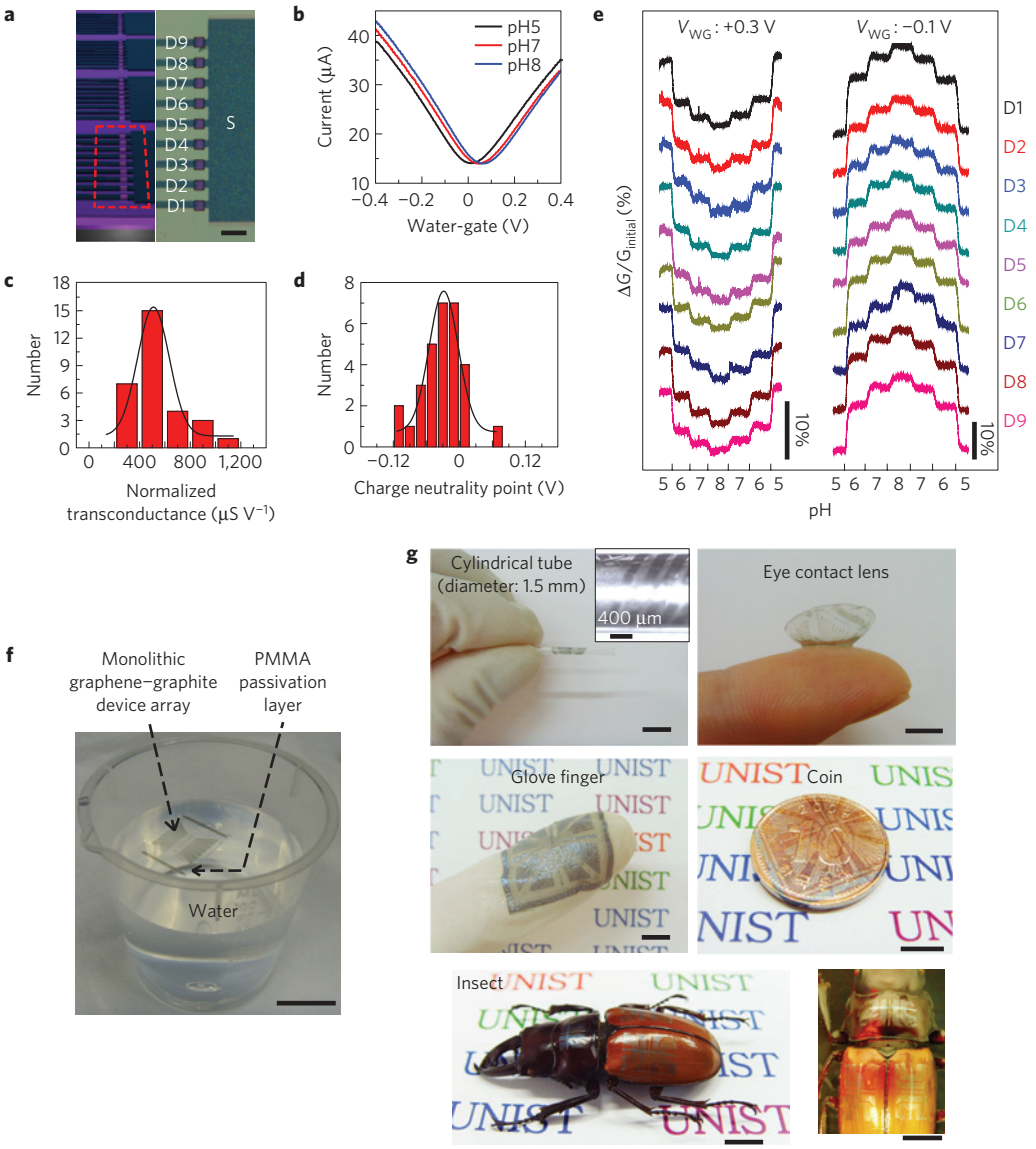

Figure 3 | Real-time, multiplexed pH sensing using monolithic graphene field-effect sensor arrays with graphite electrodes. a, Schematic illustration (left panel) of the pH sensor array. Nine individual FETs compose one block, and the array has four blocks in total. An optical micrograph of one block is shown in the right panel. Scale bar, 100 μm. **b**, Water-gate characterization at different pH levels. **c**,**d**, Statistical distributions of the normalized transconductance (in the p-type regime) and charge neutrality point at pH 7. The transconductance in the n-type regime also showed similar distributions. **e**, Complementary pH sensing using nine monolithic field-effect sensors in both n-type (V_{WG}: +0.3 V) and p-type (V_{WG}: −0.1 V) regimes. V_{WG} is the water-gate potential and $G_{initial}$ is the conductance value at the starting condition (pH 5). **f**, Photograph of free-standing, monolithic graphene–graphite integrated sensor networks floating on water. Scale bar, 20 mm. Here, the array geometry is different from the form in **a**–**e**. **g**, Photographs of monolithic device structures transferred onto various non-planar substrates, such as a cylindrical glass tube (outer diameter: ~1.5 mm), eye contact lens (soft galyfilcon A polymer), glove finger, coin, and the epidermis of an insect (*Odontolabis sarasinorum* specimen). A magnified top-view image of the insect is shown on the right. Scale bars, 5 mm.

ponent. Although relatively less transparent graphite (~850 layers) was employed as S/D and interconnects (Fig. 4) to facilitate alignment of the top-gate patterns using a conventional mask aligner, the transmittance of the final devices can be enhanced further with lower *n*.

The statistical distributions of the charge neutrality point and transconductance of the top-gate FET arrays (average mobility: 675 $cm^2 V^{-1}s^{-1}$) are provided in Fig. 4c, and these data fit Gaussian profiles. Compared with the back-gate FETs in Fig. 2, the charge neutrality point shifted close to zero, probably because of oxygen desorption from graphene in the SiO_2 evaporation step. Last, we studied the mechanical flexibility of our monolithic graphene–graphite top-gate FET devices. Figure 4d presents current (I_D) versus top-gate voltage (V_G) curves of the FET when the substrate was flat and when it was bent (radius of curvature: 0.7 cm), clearly showing no significant change in the electrical response (mobility values remained constant) as a result of bending to radii of curvature as small as 0.7 cm (estimated bending-induced strain: ~0.6%). The electrical properties of the monolithic graphene–graphite devices remain almost constant when applying a maximum strain of ~4%, demonstrating the unique mechanical flexibility of our monolithic graphene–graphite integrated electronics (Supplementary Fig. S9).

Chemical synthesis of monolithic graphene–graphite electronics exhibits unique features compared with conventional Si-based fabrication and integrated electronics. From a materials synthesis perspective, our chemical synthesis of the entire graphene–graphite integrated electronics demonstrates the encoding of distinct

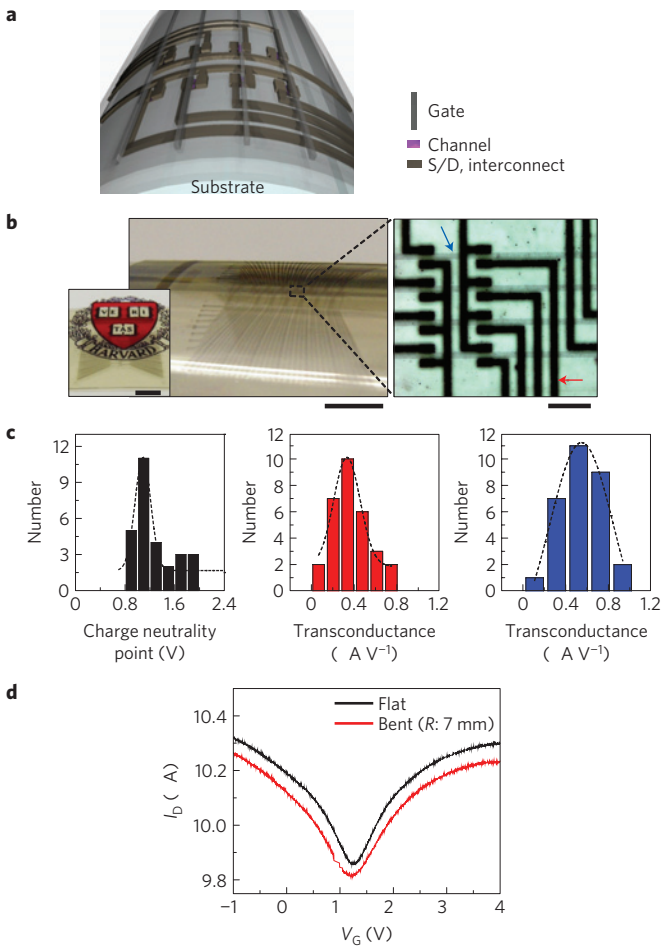

Figure 4 | Flexible and semitransparent top-gate monolithic graphene–graphite FET arrays. a, Schematic illustration of the device layout. **b**, Photograph (main panel) of the devices wrapped on a cylindrical glass (radius of curvature: 1.2 cm). The device is rested on a paper printed with a logo to demonstrate the semitransparent characteristics of the monolithic graphene–graphite devices (left inset). Scale bars, 4 mm. Optical micrograph of the top-gate FET arrays (right image). Scale bar, 200 μm. The blue arrow indicates the top-gate line and the red arrow indicates the S/D with interconnects. **c**, Statistical distributions of the charge neutrality point (left panel) and transconductance in the n-type (centre) and p-type (right) regimes. **d**, I_D–V_G curves of the top-gate FET measured when the substrate is flat and when it is bent (radius of curvature: 0.7 cm).

electronic functionalities by synthetic control of the graphene layers and also simplifies the intensive fabrication steps (for example, lithography, ion-implantation, annealing, deposition, etching, and so on) necessary for conventional Si-based electronics. From a device perspective, the monolithic graphene–graphite structure offers unique potential for flexible electronics/sensors. In contrast to conventional integrated electronics, which have mechanically fragile heterogeneous metal–semiconductor interfaces, our monolithic graphene–graphite devices demonstrate a superb mechanical flexibility based on their monolithic interface that could be further explored up to the extent of the intrinsic mechanical properties of graphene/graphite[10]. Furthermore, the high thermal conductivity (in-plane) and transparent electrical contacts of the monolithic geometry could be advantageous in enhancing heat dissipation during device operation.

We believe the capability to synthesize monolithic graphene–graphite integrated electronics provides a promising strategy towards flexible, wearable electronics and implantable biosensor devices, and also indicates the substantial promise of future graphene-based electronics in both two and three dimensions.

Methods

Spatially patterned, heterogeneous metal catalyst films were prepared by photolithography and thermal evaporation, and atmospheric CVD was carried out to synthesize the monolithic graphene–graphite structures. After the metal layers were removed in solution, the monolithic graphene–graphite structures were transferred onto Si substrates with 285 nm thick SiO_2. For the fabrication of monolithic top-gate FETs, a 400 nm-thick SiO_2 layer was evaporated as a gate dielectric and a graphite film (6–8 graphene layers) was transferred and patterned as the top-gate electrodes. Current versus back-gate and top-gate measurements were conducted with a probe station (model 12561B, Cascade Microtech) equipped with a computer-controlled analog-to-digital converter (model 6030E, National Instruments) and a variable gain amplifier (1211 current preamplifier, DL Instruments). Multichannel pH sensing was carried out with custom-designed variable gain amplifiers (multi-channel current preamplifier, SciMath Systems, LLC) and filtered using computer-based virtual lock-in amplifiers (multiplex 128-channel digital lock-in amplifier set-up kit, National Instruments).

Received 5 January 2011; accepted 13 October 2011; published online 20 November 2011

References

1. Lu, W. & Lieber, C. M. Nanoelectronics from the bottom up. *Nature Mater.* **6,** 841–850 (2007).
2. Dai, H. Carbon nanotubes: Synthesis, integration, and properties. *Acc. Chem. Res.* **35,** 1035–1044 (2002).
3. Yang, C., Zhong, Z. & Lieber, C. M. Encoding electronic properties by synthesis of axial modulation-doped silicon nanowires. *Science* **310,** 1304–1307 (2005).
4. Lauhon, L. J., Gudiksen, M. S., Wang, D. & Lieber, C. M. Epitaxial core–shell and core–multishell nanowire heterostructures. *Nature* **420,** 57–61 (2002).
5. Kocabas, C., Shim, M. & Rogers, J. A. Spatially selective guided growth of high-coverage arrays and random networks of single-walled carbon nanotubes and their integration into electronic devices. *J. Am. Chem. Soc.* **128,** 4540–4541 (2006).
6. Zhou, W., Ding, L., Yang, S. & Liu, J. Orthogonal orientation control of carbon nanotube growth. *J. Am. Chem. Soc.* **132,** 336–341 (2010).
7. Novoselov, K. S. *et al.* Two-dimensional gas of massless Dirac fermions in graphene. *Nature* **438,** 197–200 (2005).
8. Zhang, Y., Tan, Y., Stormer, H. L. & Kim, P. Experimental observation of the quantum Hall effect and Berry's phase in graphene. *Nature* **438,** 201–204 (2005).
9. Novoselov, K. S. *et al.* Electric field effect in atomically thin carbon films. *Science* **306,** 666–669 (2004).
10. Lee, C., Wei, X., Kysar, J. W. & Hone, J. Measurement of the elastic properties and intrinsic strength of monolayer graphene. *Science* **321,** 385–388 (2008).
11. Seol, J. H. *et al.* Two-dimensional phonon transport in supported graphene. *Science* **328,** 213–216 (2010).
12. Nair, R. R. *et al.* Fine structure constant defines visual transparency of graphene. *Science* **320,** 1308–1308 (2008).
13. Levendorf, M. P., Ruiz-Vargas, C. S., Garg, S. & Park, J. Transfer-free batch fabrication of single layer graphene transistors. *Nano Lett.* **9,** 4479–4483 (2009).
14. Kim, K. S. *et al.* Large-scale pattern growth of graphene films for stretchable transparent electrodes. *Nature* **457,** 706–710 (2009).
15. Jobst, J., Waldmann, D., Emtsev, K. V., Seyller, Th. & Weber, H. B. Transport properties of single-layer epitaxial graphene on 6H-SiC (0001). *Mater. Sci. Forum* **645–648,** 637–641 (2010).
16. Mattevi, C., Kim, H. & Chhowalla, M. A review of chemical vapour deposition of graphene on copper. *J. Mater. Chem.* **21,** 3324–3334 (2010).
17. Li, X. *et al.* Large-area synthesis of high-quality and uniform graphene films on copper foils. *Science* **324,** 1312–1314 (2009).
18. Reina, A. *et al.* Large area, few-layer graphene films on arbitrary substrates by chemical vapor deposition. *Nano Lett.* **9,** 30–35 (2009).
19. Jauregui, L. A., Cao, H., Wu, W., Yu, Q. & Chen, Y. P. Electronic properties of grains and grain boundaries in graphene grown by chemical vapor deposition. *Solid State Commun.* **151,** 1100–1104 (2011).
20. Han, M. Y., Ozyilmaz, B., Zhang, Y. & Kim, P. Energy band-gap engineering of graphene nanoribbons. *Phys. Rev. Lett.* **98,** 206805 (2007).
21. Li, X., Cai, W., Colombo, L. & Ruoff, R. S. Evolution of graphene growth on Ni and Cu by carbon isotope labeling. *Nano Lett.* **9,** 4268–4272 (2009).
22. Blake, P. *et al.* Making graphene visible. *Appl. Phys. Lett.* **91,** 063124 (2007).
23. Dresselhaus, M. S., Jorio, A., Hofmann, M., Dresselhaus, G. & Saito, R. Perspectives on carbon nanotubes and graphene Raman spectroscopy. *Nano Lett.* **10,** 751–758 (2010).

24. Bae, S. *et al.* Roll-to-roll production of 30 inch graphene films for transparent electrodes. *Nature Nanotech.* **5,** 574–578 (2010).
25. Bhaviripudi, S., Jia, X., Dresselhaus, M. S. & Kong, J. Role of kinetic factors in chemical vapor deposition synthesis of uniform large area graphene using copper catalyst. *Nano Lett.* **10,** 4128–4133 (2010).
26. Zhang, Y., Small, J. P., Pontius, W. V. & Kim, P. Fabrication and electric-field-dependent transport measurements of mesoscopic graphite devices. *Appl. Phys. Lett.* **86,** 073104 (2005).
27. Yazyev, O. V. & Louie, S. G. Electronic transport in polycrystalline graphene. *Nature Mater.* **9,** 806–809 (2010).
28. Dean, C. R. *et al.* Boron nitride substrates for high-quality graphene electronics. *Nature Nanotech.* **5,** 722–726 (2010).
29. Ohno, Y., Maehashi, K., Yamashiro, Y. & Matsumoto, K. Electrolyte-gated graphene field-effect transistors for detecting pH and protein adsorption. *Nano Lett.* **9,** 3318–3322 (2009).
30. Cohen-Karni, T., Qing, Q., Li, Q., Fang, Y. & Lieber, C. M. Graphene and nanowire transistors for cellular interfaces and electrical recording. *Nano Lett.* **10,** 1098–1102 (2010).

Acknowledgements

We thank L. Wang for assistance on electrical measurements, Y. K. Kim for TEM characterization, and J. Cahoon and Q. Qing for helpful discussions. J-U.P. thanks UNIST for support through the 2010 Research Fund, and S.N. thanks the Samsung Scholarship. This research was supported by a research project of National Research Foundation of Korea (Grant number: 20110014111), and by a NIH Director's Pioneer Award (5DP1OD003900).

Author contributions

J-U.P., S.N. and C.M.L. designed the experiments. J-U.P., S. N. and M-S. L. performed the experiments. J-U.P., S.N. and C.M.L. analysed the data and wrote the paper.

Additional information

The authors declare no competing financial interests. Supplementary information accompanies this paper on www.nature.com/naturematerials. Reprints and permissions information is available online at http://www.nature.com/reprints. Correspondence and requests for materials should be addressed to J-U.P. or S.N.